PAPER

High-efficiency design and optimization of 2 T monolithic polymer/polymer tandem solar cells using SCAPS-1D simulations

To cite this article: Samia Moulebhar *et al* 2025 *Phys. Scr.* **100** 045108

Physica Scripta

PAPER

High-efficiency design and optimization of 2 T monolithic polymer/polymer tandem solar cells using SCAPS-1D simulations

Samia Moulebhar[1,2], **Chahrazed Bendenia**[1,2], **Souhila Bendenia**[2], **Hanaa Merad-Dib**[2], **Sid Ahmed Khantar**[1,2] **and Sarra Merabet**[1,2]

[1] Laboratory of Electromagnetism and Guided Optics, Faculty of Science and Technology University Abd El Hamid Ibn Badis, Mostaganem 27000, Algeria

[2] Analysis, Modeling,Advanced Materials for Renewable Energies Laboratory, Faculty of Science and Technology, University Abd El Hamid Ibn Badis, Mostaganem 27000, Algeria

E-mail: samiamoulebhar@gmail.com

RECEIVED
25 December 2024

REVISED
17 February 2025

ACCEPTED FOR PUBLICATION
7 March 2025

PUBLISHED
20 March 2025

Keywords: organic solar cell, tandem, performances, SCAPS 1D

Abstract

In this study, we present a novel 2 T monolithic polymer/polymer tandem solar cell (TSC) model based on experimentally validated sub-cell designs composed entirely of OSC/OSC polymers. The individual sub-cells have been calibrated against experimental data, resulting in power conversion efficiencies (PCE) of 10.33% for the front cell and 21.72% for the back cell. The lower cell contains a PM6:Y6 active layer in an ITO/Cu2O/PM6:Y6/SnO2/Ag configuration, while the upper polymer cell is designed with a conventional ITO/PEDOT:PSS/PM7:PIDT/PDINN/Ag structure, with PM7:PIDT as the absorber layer. Simulations were performed using the 1D SCAPS tool to individually optimize the performance of each sub-cell. Extensive investigation was carried out on band alignment, defect density, active layer thickness and the selection of electron and hole transport layers (ETLs and HTLs). The effects of temperature, shunt resistance and series resistance on the two sub-cells were also analyzed to improve stability and performance. The resulting tandem structure exhibited a short circuit current density (J_{SC}) of 11.685 mA cm^{-2}, an open circuit voltage (V_{OC}) of 2.0721 V, a fill factor of 82.823% and a PCE of 20.054%, positioning it as a promising candidate for flexible, green and highly efficient tandem solar cells. These results highlight the potential of our design to advance the performance benchmarks of organic tandem solar cells.

Nomenclature table with units.

Nomenclature	Meaning	Units
HTL	Hole Transport Layer	
ETL	Electron Transport Layer	
E_g	Energy Bandgap	(eV)
χ	Electron Affinity	(eV)
ε	Relative Permittivity	
N_c	Effective Density of States in Conduction Band	$(1/cm^3)$
N_v	Effective Density of States in Valence Band	$(1/cm^3)$
μ_e	Electron Mobility	$(cm^2/V{\cdot}s)$
μ_h	Hole Mobility	$(cm^2/V{\cdot}s)$
N_A	Acceptor Concentration	$(1/cm^3)$
N_d	Donor Concentration	$(1/cm^3)$
N_t	Trap Density	$(1/cm^3)$
PCE	Efficiency	(%)
J_{SC}	Short circuit density	$(mA.cm^{-2})$
FF	Fill Factor	(%)
V_{OC}	Open Circuit voltage	(V)

1. Introduction

Recently, solar energy production has grown rapidly to become the most abundant form of renewable energy. Against this backdrop, photovoltaic (PV) technologies have made great strides, leading to the development of new materials and structures that improve efficiency and reduce processing costs [1–3]. A notable advance in this generation of solar cells is the organic solar cell (OSC), which has attracted considerable interest from researchers due to its unique properties. They offer low manufacturing costs, as well as being lightweight, flexible, energy-efficient and suitable for large-scale printing [4–7]. The efficiency with which organic solar cells convert electricity, known as power conversion efficiency (PCE), has improved significantly, rising from less than 10% in 2017 to around 17% recently [8–11]. Despite these advances, OSCs still face challenges such as relatively low current density (JSC) and high energy losses, which need to be addressed for their further development [12]. In addition, the performance of associated cells remains limited because a single junction can only absorb photons with energy equal to or greater than the bandgap energy of the photoactive materials used. Due to the thermalization process, not every incoming photon is absorbed; higher energy photons end up losing their excess energy to photons in the remaining spectrum [8, 13, 14] . A recent promising strategy developed in thin films to meet the high demands of energy conversion efficiency and low fabrication cost is the use of multi-junction architectures, where the structure of tandem solar cells is based on sub-cells using different absorber materials to capture a large part of the incident spectrum. Tandems can be composed of two or more complementary materials, allowing the power spectrum to be split between multiple absorbers. A typical two-junction tandem configuration consists of an upper wide bandgap sub-cell, which absorbs short wavelength photons, and a lower narrow bandgap sub-cell, which captures long wavelength photons [15, 16]. Tandem cells can be constructed with two different sub-cells using various techniques, including mechanical stacking of devices with four terminals (4 T), spectrum splitting with three terminals (3 T) or two terminals (2 T) on a monolithic device. These sub-cells are electrically connected by an intermediate layer called the recombination layer, which can be an ultrathin film of a metal such as silver (Ag). In 2020, Yang *et al* [17] showed that the use of Ag improved efficiency, stability and reduced voltage losses (0.04 V) thanks to good ohmic contact between the ICL and the sub-cells. In 2 T tandem devices, the primary electrical constraint is current, as the power is limited by the current corresponding to the sub-cells [18]. Furthermore, sub-cells connected in series can significantly reduce electrical losses due to excessive current flow through the current collector [19]. Due to their sub-cell composition, tandem solar cells outperform single-junction devices by efficiently absorbing a wider range of wavelengths across the electromagnetic spectrum. Consequently, the use of tandem OSCs represents a potential solution for improving PCE. All-polymer bulk heterojunction solar cells (all-OSCs) using polymerized small molecule acceptors (PSMAs) have made significant progress due to their mechanical stability, thermal resistance and environmental friendliness [20]. The first PSMA, PZ1, achieved an efficiency of 9.19% [21]. Since then, the efficiency of all-PSCs has improved, recently reaching over 18%. Experimental studies of all-polymer tandem solar cells have shown promising results, with efficiencies ranging from 6.70% to 17.87% across different configurations and polymer combinations [22]. For example, in this configuration, the top sub-cell consisted of a wide bandgap polymer (PIDT) with a bandgap energy of 1.66 eV, while the bottom sub-cell used a narrow bandgap polymer (PY-IT) with a bandgap energy of 1.40 eV. The two sub-cells used polymer donors PM7 and PM6 respectively. The optimum power conversion efficiency (PCE) achieved for this tandem device was 17.87% with the following structure: ITO/PEDOT/PM7:PIDT/C60/BPhen/PEDOT:PSS/PM6: PYIT/PDINN/Ag [12].

Our research introduces a new tandem structure, where the two sub-cells are inspired by models already studied experimentally. These models have been calibrated and validated against experimental data, using two reference cells composed exclusively of OSC/OSC polymers. This innovative approach makes it possible to explore new structural configurations to optimize the performance of organic solar cells, while building on empirically verified foundations. The bottom cell is designed with the PM6 :Y6 as the active layer and is configured with the following structure: ITO/Cu2O/PM6:Y6/SnO2/Ag [23], Meanwhile, the top polymer cell features a p-i-n structure that is comprised of ITO/PEDOT:PSS/PM7:PIDT/PDINN/Ag [12].

In this study we simulated the two sub-cells separately using the SCAPS 1D tool. The top cell showed a short-circuit current of 11.47 mA cm^{-2}, an open-circuit voltage of 1.1455 V, a fill factor of 78.56% and a power conversion efficiency of 10.33%, while the bottom cell showed a short-circuit current of 30.462 mA cm^{-2}, an open-circuit voltage of 0.9257 V, a fill factor of 77.02% and a power conversion efficiency of 21.72%. We first studied the band structures of the two sub-cells, in order to understand their interaction and optimize their operation in the tandem cell. We then examined the impact of defect density and variation in active layer thickness on the overall performance of the cell. In addition, an in-depth study was carried out on different types of electron transport layers (ETLs) and hole transport layers (HTLs) to improve the performance of both the top cell (T_{CELL}) and the bottom cell (B_{CELL}). We have also investigated the effect of temperature variations on the efficiency of the tandem cell, as well as the influence of shunt and series resistances, two essential parameters for

optimizing the performance and stability of tandem solar cells. The proposed tandem structure finally achieved a short circuit current of 11.685 mA cm^{-2}, an open circuit voltage of 2.0721 V, a fill factor of 82.823% and a power conversion efficiency of 20.054%, results that compare favorably with those reported in the literature.

2. Simulation approach and device configuration

2.1. Simulation software

The SCAPS-1D simulator is used to calculate the photovoltaic (PV) characteristics of the organic solar cells (OSCs) under investigation. The simulation is based on the fundamental principles of semiconductor physics, in particular Poisson's equation and the continuity equations for both electrons and holes. These equations (Poisson's equation as equation (1) and the continuity equations as equations (2) and (3)) are fundamental in describing the behavior of charge carriers within the solar cell.

The simulation takes into account various loss mechanisms, including Shockley-Read-Hall (SRH) recombination, which is critical to the accurate determination of PV parameters. The symbols used in these equations are defined and explained to ensure a clear understanding of the calculations [24, 25].

$$\frac{\partial^2\omega}{\partial x^2} + \frac{q}{\varepsilon}[\rho(x) - n(x) + N_D - N_A + \rho_p + \rho_n\ ] = 0 \tag{1}$$

$$\frac{1}{q}\frac{dJ_p}{dx} = G_{op}(x) - \mathrm{R(x)} \tag{2}$$

$$\frac{1}{q}\frac{dJ_n}{dx} = -G_{op}(x) + \mathrm{R(x)} \tag{3}$$

Where ω and ε represent the electrostatic potential and the permittivity, respectively, while ρ and q represent density and elementary charge, respectively. N_{d+} is the concentration of donor-ionized doping, and N_{A-} is the concentration of acceptor-ionized doping. ρ_p, ρ_n, J_n, and J_p represent the electron and hole diffusion coefficients and the electron and hole current densities, respectively.

2.2. Top and bottom sub cell calibration

The tandem cell created is based on sub-cells that have been practically designed and executed. for our proposal design The front sub-cell is an OSC with a band gap of 1.76 eV, while the rear sub-cell has a band gap of 1.4 eV, as shown in the following diagram in figure 1 [26] .The upper sub-cell cell was constructed with an ITO front contact (work function = 4.6 eV). For the hole transport layer (HTL), a layer of p-type doped PEDOT:PSS with an energy bandgap (E_g) of 1.60 eV, an electron affinity of 3.60 eV and an acceptor doping concentration (N_A) of 9×10^{20} cm^{-3} was used. The light absorption layer consists of a polymerized small molecule acceptor of PIDT, combined with a polymer donor of PM7 (undoped, 100 nm thick, with an optical bandgap of 1.76 eV and an electron affinity of 3.74 eV).The electron transport layer (ETL) is formed from n-type PDINN, 30 nm thick, with an energy bandgap (E_g) of 2.24 eV, an electron affinity of 3.78 eV and a donor doping concentration (N_D) of 9×10^{19} cm^{-3}. Finally, a silver (Ag) back contact with a work function of 4.2 eV was used due to its exceptional electrical conductivity, high reflectivity, and chemical stability, which contribute to efficient charge collection, enhanced photon management, and long-term device stability [2].The lower sub-cell is based on a PM6:Y6 as absorber layer, with an undoped bandgap of 1.27 eV, 100 nm thick, and an energy band gap (E_g) of 1.4 eV, with an electron affinity of 4.1 eV. This absorber layer enhances performance due to the minimal energy difference between the highest occupied molecular orbital (HOMO) of the donor (PM6) and the acceptor (Y6) [27]. For the electron transport layer (ETL), tin oxide (SnO_2) is employed as the n-type material. SnO_2 has a high band gap of 3.4 eV, a thickness of 150 nm, an electron affinity of 3.40 eV, and an acceptor doping concentration (N_A) of 2.2×10^{16} cm^{-3}.

The hole transport layer (HTL) consists of Cu_2O, having a band gap of 2.17 eV, p-type, with a thickness of 150 nm, an electron affinity of 3.20 eV, and an acceptor doping concentration (N_A) of 1×10^{18} cm^{-3}. The tandem sub-cells are cells are connected in series separated by an intermediate layer (ICL). This interlayer may be either a very thin metal layer or a film of transparent conductive oxide in order to optimize absorption and energy conversion, with each photoactive unit designed to exploit different spectral ranges [28, 29].

The spectrum transmitted from the front sub-cell to the rear sub-cell is described by (4), while the absorption coefficient (α) of each material in the layer is specified by (5) [30].

$$\mathrm{S}(\lambda) = \mathrm{S}_0(\lambda) \cdot \prod_{x=1}^{n} e^{-\alpha_x d_x} \tag{4}$$

$$\alpha(\mathrm{E}) = \mathrm{A} \cdot \sqrt{\mathrm{h}\nu - \mathrm{Eg}} \tag{5}$$

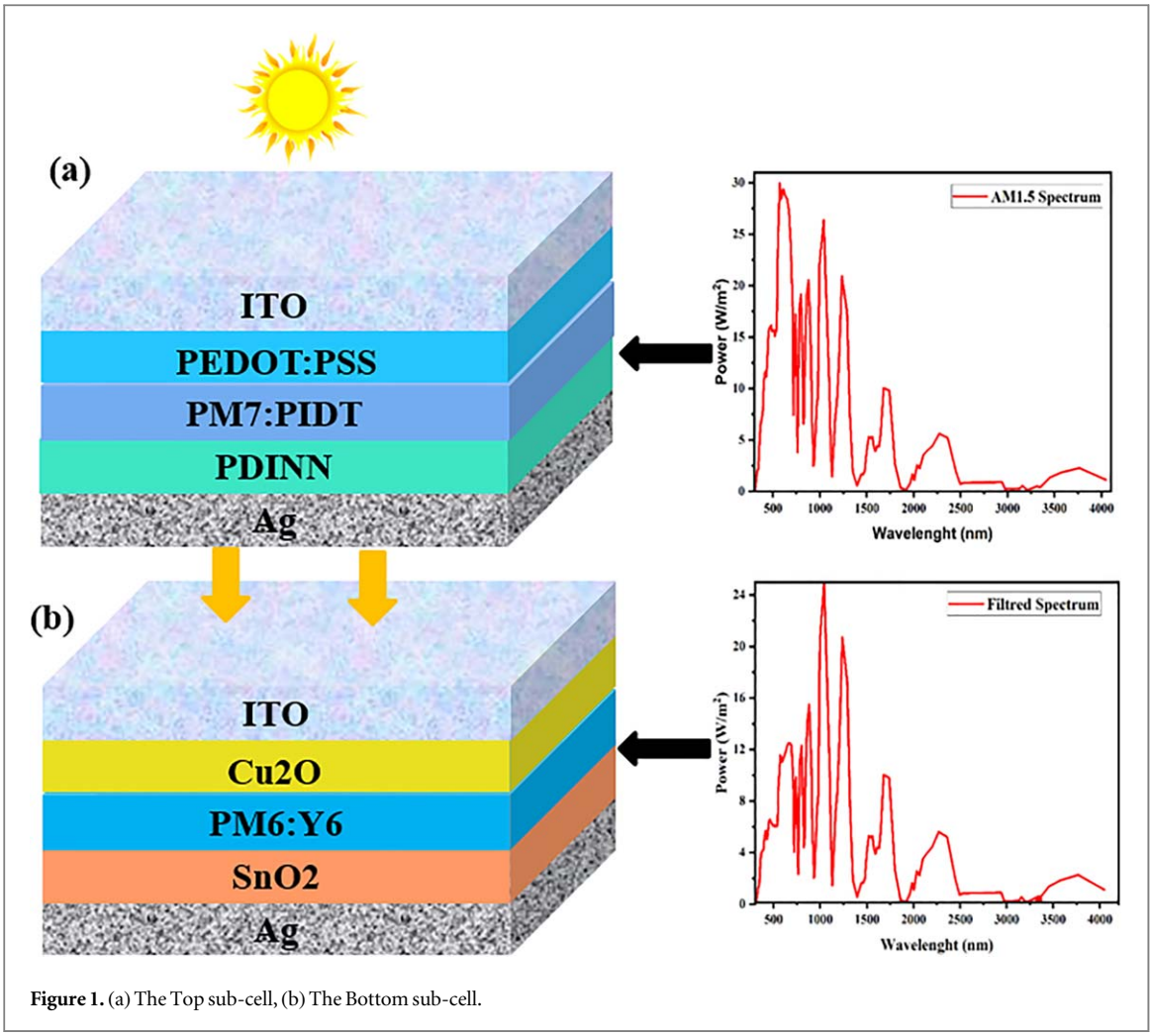

Figure 1. (a) The Top sub-cell, (b) The Bottom sub-cell.

The physical and geometrical properties of the layers are derived from the latest experimental data and previous studies and are detailed in tables 1 and 2. These tables include information on layer thicknesses, band gaps, doping levels, defect densities and interface properties [31]. Defect types and layer densities are held constant, while thicknesses and doping concentrations are adjusted for optimization, ensuring a precise match between the lower and upper sub-cells. The simulations use an incident power density of 1000 mW cm^{-2} with an AM 1.5 spectrum.

3. Results and discussions

3.1. Independent simulation of T_{CELL} and B_{CELL} sub-cells

In this section, we simulated the two sub-cells, the T_{CELL} and the B_{CELL}, separately under the AM1.5 spectrum. In addition, the B_{CELL} was simulated under a filtered spectrum, representing the light transmitted after absorption by the T_{CELL}. The results of this simulation are presented in table 3 and are compared with previous experimental and simulation works.

3.2. Band alignment of upper and lower sub cell

The alignment of energy bands is crucial for solar cell performance. Figure 2 displays the band alignment diagrams for both the upper and lower sub-cells [33]. Essential to the effective operation of solar cells is the conduction band offset (CBO) between the absorber and the electron transport layer (ETL) in a heterojunction. Charge transfer and recombination mechanisms within the tandem cell are significantly affected by variations in band alignment due to positive or negative CBO values. A negative CBOs increases the flow of electrons, improving device performance, whereas a positive CBOs creates a barrier to electron transfer, reducing charge extraction efficiency and increasing the probability of hole–electron recombination at the cell interface, leading to reduced device efficiency. Similarly, the operation of tandem solar cells is greatly affected by the valence band

Table 1. Different layer optoelectronic parameters input.

Parameteres	Bottom cell [23]			Top cell [2, 12]		
	HTL	Active layer	ETL	HTL	Active layer	ETL
Materials	Cu2O	PM6: Y6	SnO2	PEDOT: PSS	PM7: PIDT	PDINN
Thickness (μm)	0.150	100	0.01	0.03	100	0.03
E_g (eV)	2.17	1.4	3.2	1.6	1.76	2.24
χ (eV)	3.2	4.1	4.2	3.6	3.74	3.78
ε (relative)	7.1	3.8	3.9	3	3	5
Nc ($1.cm^{-3}$)	2×10^{17}	2.5×10^{21}	2.2×10^{17}	1e21	1×10^{21}	1×10^{19}
Nv ($1.cm^{-3}$)	1.1×10^{19}	2.5×10^{21}	2.2×10^{16}	1e21	1×10^{21}	1×10^{19}
μ_e (cm^2/Vs)	200	2.5×10^{-4}	20	4.5×10^{4}	2.89×10^{-4}	2×10^{-6}
μ_h (cm^2/Vs)	80	2.5×10^{-4}	20	9.9×10^{-5}	2.89×10^{-4}	1×10^{-3}
N_A ($1.cm^{-3}$)	1×10^{18}	0	0	9×10^{21}	0	0
N_D ($1.cm^{-3}$)	0	0	2.2×10^{16}	0	0	1×10^{22}
N_t(($1.cm^{-3}$)	1×10^{14}	0	1×10^{15}	1×10^{13}	0	1×10^{13}

Table 2. Attributes of T_{CELL} and B_{CELL} interface defects.

Parameters	Bottom cell		Top cell	
Defect type	Cu2O/PM6:Y6 Neutral	PM6:Y6/SnO2 Neutral	PEDOT:PSS/PM7:PIDT Neutral	PDINN/PM7:PIDT Neutral
Electron capture cross-section (cm^2)	1×10^{-19}	1×10^{-19}	1×10^{-19}	1×10^{-19}
Hole capture cross-section (cm^2)	1×10^{-19}	1×10^{-19}	1×10^{-19}	1×10^{-19}
Energy level above Ev (eV)	0.6	0.6	0.6	0.6
Concentration (N_t) (cm^{-3})	1×10^{11}	1×10^{11}	1×10^{10}	1×10^{10}

Table 3. Performance metrics of top and bottom sub-cells compared to other experimental and simulation works.

PV Parameters	Jsc($mA.cm^2$)	Voc(V)	FF(%)	PCE(%)	Tools	References
Bottom Cell	37.497	0.9346	70.21	24.60	SCAPS-1D	[23]
	27.48	0.84	79.0	18.38	Experimental	[32]
	30.462	0.9257	77.02	21.72	SCAPS 1D	This work
Top Cell	14	1.1	65.3	10.1	Experimental	[12]
	13.76	1.10	66.76	10.110	Tcad	[26]
	11.47	1.1455	78.56	10.33	SCAPS 1D	This work

offset (VBO) between the absorber and the hole transport layer (HTL) in a heterojunction. Changes in VBO can profoundly influence charge transfer and recombination processes within the device [22, 34].

The Anderson model can be used to calculate the conduction band offset (CBO) and valence band offset (VBO) for the hole transport layer (HTL), electron transport layer (ETL), and the active layer. According to this model, the offsets are determined by the following calculation:

$$\mathrm{CBO} = (\chi_{\text{Active layer}} - \chi_{\mathrm{ETL}}) \tag{6}$$

$$\mathrm{VBO} = (\chi_{\mathrm{HTL}} - \chi_{\text{Active layer}}) + (\mathrm{Eg}_{\mathrm{HTL}} - \mathrm{Eg}_{\text{Active layer}}) \tag{7}$$

In our tandem cell configuration, we selected PDINN as the ETL for the upper cell, with a CBO of −0.04 eV, as shown in figure 2(a). Similarly, we used SnO_2 as the ETL for the lower cell, with a CBO of −0.1 eV, as indicated in figure 2(b). This favorable band alignment enhances charge extraction and reduces recombination at the interface between the upper and lower cells. For the VBO, we chose PEDOT:PSS as the HTL for the upper cell, with a VBO of −0.03 eV, as depicted in figure 2(a). For the lower cell, we employed Cu_2O as the HTL, with a VBO of −0.43 eV, as shown in figure 2(b).

3.3. Effect of functional organic layer thickness and defect density

To optimize the performance of T_{CELL} (1.73 eV) and B_{CELL} (1.4 eV) cells, an in-depth study of photovoltaic parameters was conducted using SCAPS-1D. we study the impact of different defect densities (10^7 cm^{-3} to 10^{13} cm^{-3}), with variations in thickness (0.1 to 0.8 μm) on the performance parameters: PCE, V_{OC}, J_{SC} and FF. Figures 3(a)–(d) illustrate the simultaneous variations in performance metrics of the T_{CELL} as functions of active

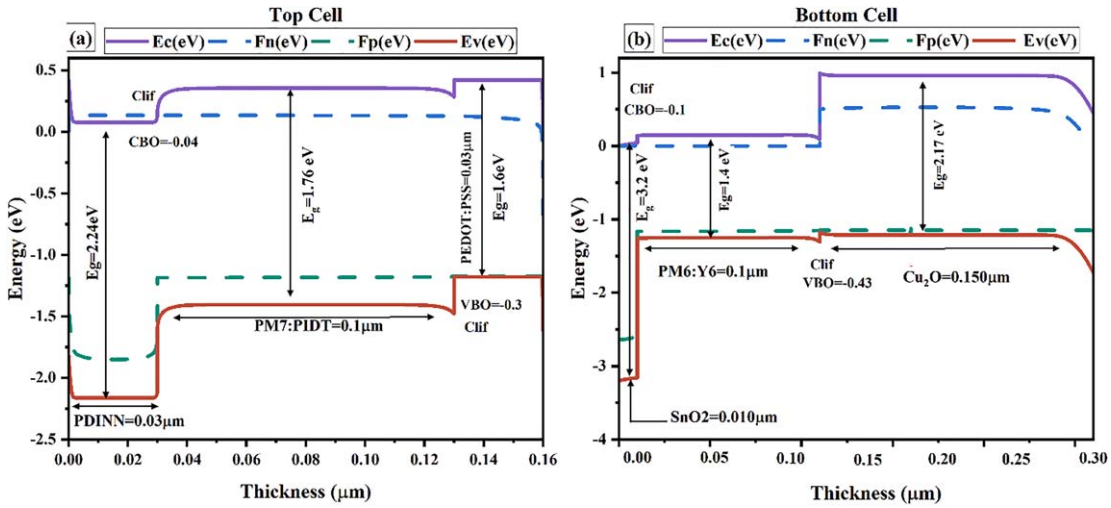

Figure 2. Energy band diagram of (a) Top cell, (b) Bottom cell.

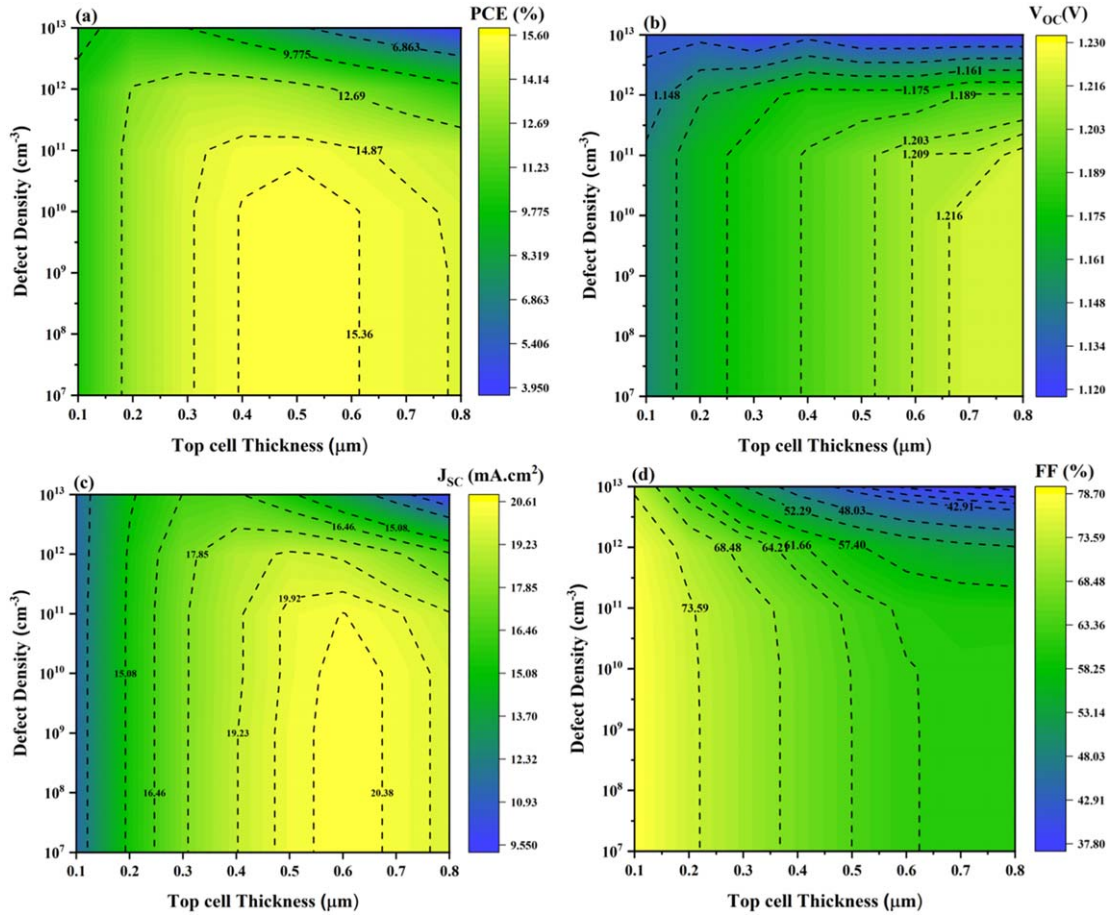

Figure 3. Impact of T_{CELL} absorber thickness and defect density on (a) PCE, (b) V_{OC}, (c) J_{SC}, (d) FF.

layer thickness and defect density. For defects from 10^{7} cm^{-3} to 10^{10} cm^{-3}, the efficiency increases with thickness, reaching a maximum of around 15.6% for a thickness of 0.50 µm and 0.60 µm. From 10^{11} cm^{-3}, a gradual decrease in efficiency is observed in figure 3(a), peaking at just 4.84% for a thickness of 0.70 µm and 0.80 µm at 10^{13} cm^{-3}. The open circuit voltage (V_{OC}) remains relatively stable between 1.15 and 1.22 V for defects up to 10^{10} cm^{-3}. At defect levels of 10^{12} cm^{-3} and 10^{13} cm^{-3}, V_{OC} decreases slightly, reaching 1.12 V. The current density J_{SC} increases with thickness for all defect levels up to 10^{10} cm^{-3}. The maximum is reached at 20.62 mA

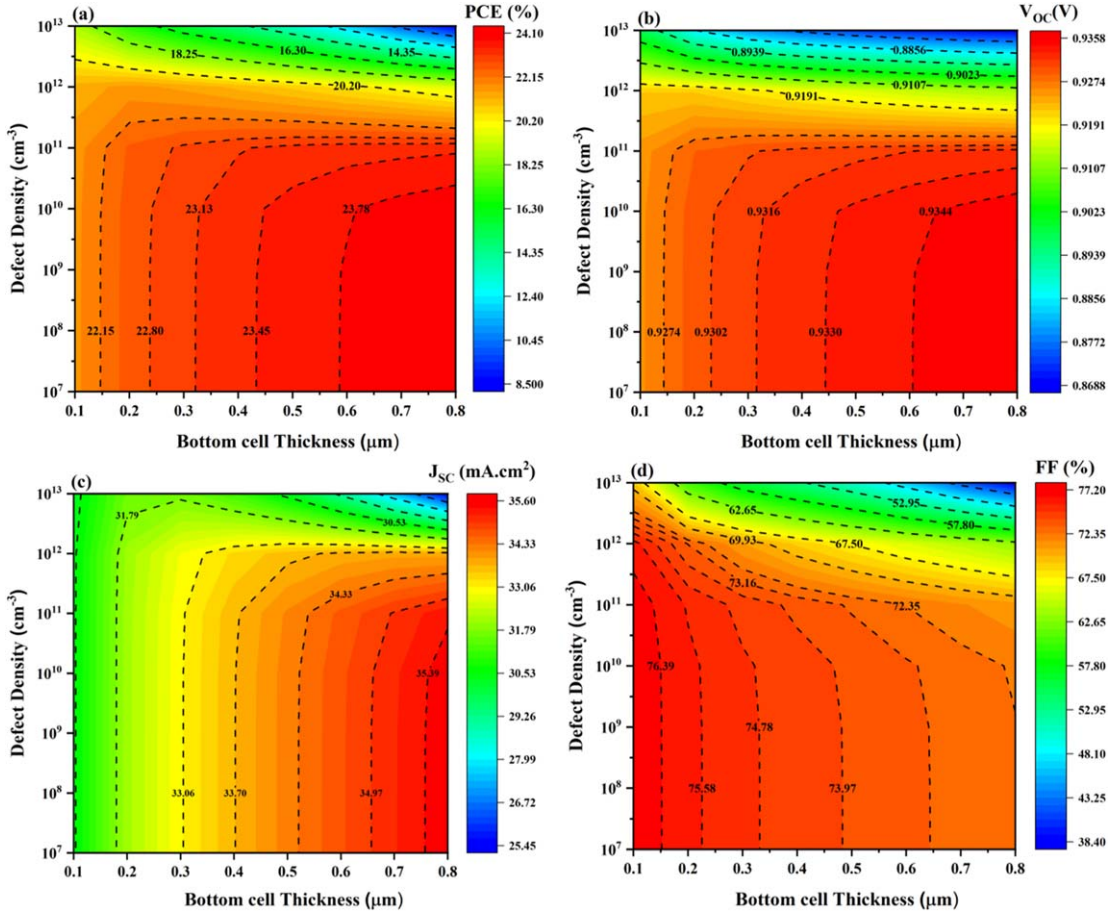

Figure 4. Impact of $_{BCELL}$ absorber thickness and defect density on (a) PCE, (b) V_{OC}, (c) J_{SC}, (d) FF.

cm^{-2} for a thickness of 0.60 μm from 10^{11} cm^{-3}, a gradual decrease in J_{SC} is observed, especially at 10^{13} cm^{-3}, where the current density drops to 9.59 mA cm^{-2}. The fill factor is high (around 78.67%) for small defects, but decreases with increasing defects and thickness. For defects of 10^{12} cm^{-3} and 10^{13} cm^{-3}, FF drops to 52.5% and 36.93%, respectively, at high defect levels, the ability of the material to perform its optimum functions is compromised, which is reflected in a sharp drop in FF [35].

Figures 4(a)–(d) shows simulation results for the bottom cell, where shows a general tendency to increase with thickness up to a certain point, followed by a noticeable decrease at high defect levels (from 10^{12} cm^{-3} and above). At low defect levels (up to 10^{11} cm^{-3}), the efficiency is relatively stable and increases with thickness, but drops drastically at very high defect values, especially for lower thicknesses. The V_{OC} remains relatively stable for lower defect densities (up to 10^{11} cm^{-3}) and increases slightly with increasing thickness. However, at very high defect levels (from 10^{12} cm^{-3}), a significant drop is observed, suggesting that high defects reduce the open-circuit voltage significantly. J_{SC} increases with thickness down to 0.8 μm at lower defect levels. However, at very high defect densities (from 10^{12} cm^{-3}), it decreases sharply, particularly for large thicknesses. This parameter seems more sensitive to high defect levels, with significant decreases for defect densities above 10^{12} cm^{-3}. FF decreases progressively with increasing defect density and thickness. This indicates that the quality of the device degrades with higher defect densities. At the lowest defect levels (10^{7} to 10^{11} cm^{-3}), the FF remains relatively stable but begins to fall rapidly for 10^{12} cm^{-3} and beyond. The performance improvement is attributed to the increased absorber thickness, which enhances carrier generation due to higher photo-excitation. In contrast, higher defect densities result in increased recombination, which decreases the number of charge carriers and thus reduces performance [36].

3.4. Effect of ETLs and HTLs

A thorough investigation of different electron transport layers (ETLs) and hole transport layers (HTLs) has been carried out to further enhance the T_{CELL} and B_{CELL}, as described in this subsection. Here, 8 types of electron transport layers and hole transport layers were simultaneously tested in the T_{CELL}, and B_{CELL}, the impact of these variations was evaluated. All the electrical parameters utilized at this stage are detailed in tables 4(a) and (b).

Table 4. (a) Electrical parameters for different ETLs. (b) Electrical parameters for different HTLs.

Parameters	C60 [37]	TiO2 [37]	CdS [38]	IGZO [38]	PCBM [39]	SnO2 [40]	WS2 [40]	ZnO [40]
				(a)				
E_g (eV)	1.7	3.2	2.4	3.05	2	3.6	1.8	3.3
χ (eV)	4.5	4	4.5	4.16	4	4	4	4
ε (relative)	10	9	10	10	3.9	9	9	9
N_c ($1.cm^{-3}$)	2.2×10^{18}	1.8×10^{19}	1.8×10^{19}	5×10^{18}	2.5×10^{21}	2.2×10^{18}	2.4×10^{19}	3.7×10^{18}
N_v ($1.cm^{-3}$)	1.8×10^{19}	1.8×10^{19}	1.8×10^{19}	5×10^{18}	2.5×10^{21}	1.8×10^{19}	1.8×10^{19}	1.80×10^{19}
μ_e (cm^2/Vs)	0.1	20	100	15	0.2	100	100	100
μ_h (cm^2/Vs)	0.1	10	25	0.1	0.2	25	100	25
N_A ($1.cm^{-3}$)	0	0	0	0	0	0	0	0
N_D ($1.cm^{-3}$)	1×10^{18}	1×10^{18}	1×10^{18}	$1 \times \times 10^{18}$	1×10^{18}	1×10^{18}	1×10^{18}	1×10^{18}
N_t(($1.cm^{-3}$)	1×10^{15}	1×10^{15}	1×10^{15}	1×10^{15}	1×10^{15}	1×10^{15}	1×10^{15}	1×10^{15}
Parameters	CuI [41]	CuO [41]	NiO [42]	P3HT [42]	PEDOT :PSS [43]	MoO3 [44]	GO [44]	Spiro-Ometad [44]
				(b)				
E_g (eV)	3.1	1.51	3.6	1.7	1.6	3.2	2.48	3
χ (eV)	2.1	4.07	2.1	3.5	3.4	2.2	2.3	2.2
ε (relative)	6.5	18.1	11.75	3	3	3	10	3
N_c ($1.cm^{-3}$)	2.8×10^{19}	2.2×10^{19}	2.5×10^{20}	2×10^{21}	2.2×10^{18}	2.2×10^{19}	1.8×10^{18}	2.2×10^{18}
N_v ($1.cm^{-3}$)	1×10^{20}	5.5×10^{20}	2.5×10^{20}	2×10^{21}	1×10^{19}	1.9×10^{19}	2.2×10^{18}	1.8×10^{19}
μ_e (cm^2/Vs)	100	100	0.001	1.8×10^{-3}	4.5×10^{-2}	2×10^{-4}	26	2.1×10^{-3}
μ_h (cm^2/Vs)	43.9	0.1	0.001	1.86×10^{-2}	4.5×10^{-2}	2×10^{-4}	23	2.16×10^{-3}
N_A ($1.cm^{-3}$)	1×10^{18}	1×10^{18}	1×10^{18}	1×10^{18}	1×10^{18}	1×10^{18}	1×10^{18}	1×10^{18}
N_D ($1.cm^{-3}$)	0	0	0	0	0	0	0	0
N_t(($1.cm^{-3}$)	1×10^{15}	1×10^{15}	1×10^{15}	1×10^{15}	1×10^{15}	1×10^{15}	1×10^{15}	1×10^{15}

Figures 5(a)–(d) illustrate the effect of varying ETLs and HTLs on the power conversion efficiency (PCE), open-circuit voltage (V_{OC}), short-circuit current (J_{SC}), and fill factor (FF) on T_{CELL}. The highest V_{OC} values (1.26–1.34 V) are observed when SnO_2, WS_2, ZnO, and TiO_2 are used as ETLs in combination with HTLs such as CuI and P3HT. This can be attributed to a favorable energy level alignment, which minimizes voltage losses and enhances charge extraction [45]. MoO_3 with TiO_2 or WS_2 also achieves V_{OC} values around 1.30–1.32 V, indicating efficient carrier transport [45, 46]. The highest J_{SC} values (10.48–10.73 mA cm^{-2}) are recorded when PEDOT:PSS is paired with C60 or PCBM as ETLs. This suggests that PEDOT:PSS allows superior hole extraction, probably due to its high charge mobility and optimal energy level matching [46]. In contrast, CuO results in a significantly lower J_{SC} (~7.1–8.5 mA cm^{-2}), which can be explained by its poor charge transport properties and non-ideal band alignment, leading to higher recombination losses [45]. The best FF values (up to 87%) are obtained when CuO is combined with PCBM and SnO_2, highlighting good interfacial properties and reduced recombination [45]. On the other hand, MoO_3 in combination with the same ETLs results in lower FF values (~79%–81%), suggesting that interface defects or charge mobility limitations may affect device performance [45]. The most efficient T_{CELL} configurations, reaching up to 11%, include SnO_2 and PCBM as ETLs, combined with CuI or PEDOT:PSS as HTLs. These combinations provide a balance between high V_{OC}, J_{SC}, and FF. In contrast, CuO as an HTL gives the lowest efficiencies (~2.8%–4.4%), confirming its limited suitability for high performance devices.

For a similar study carried out on the lower cell, figures 6(a)–(d) provide insight into the performance variations of different ETL/HTL combinations for the B_{CELL}. CuI as an HTL provides the highest V_{OC} values (~0.85–0.95 V) when paired with PCBM, SnO_2, or ZnO. This indicates strong energy level matching and reduced recombination. Conversely, MoO_3 and NiO as HTLs result in lower V_{OC} values (~0.50–0.72 V), which may be due to increased interfacial losses and higher series resistance [47]. The best J_{SC} values (~32–36 mA cm^{-2}) are observed when CuI or NiO are used as an HTL in combination with PCBM, SnO_2, or ZnO. These combinations enhance charge transport and minimize recombination. In contrast, CuO result in the lowest J_{SC} (~16–20 mA cm^{-2}), further confirming its poor electrical properties [47]. The highest FF values (~65%–73%) are achieved with CuI and PEDOT:PSS as HTLs in combination with PCBM and SnO_2, indicating improved charge extraction and minimal resistance losses. MoO_3 and NiO as HTLs result in lower FF values (~40%–55%), suggesting that these materials introduce higher series resistances [47]. The most efficient B_{CELL} configurations achieve PCE values of ~21%–25%, particularly with CuI as the HTL and PCBM or SnO_2 as ETLs. This highlights the superior performance of these materials in ensuring high charge transport and minimal losses. In contrast, CuO-based configurations yield the lowest efficiencies (~0.5%–4.4%), indicating poor

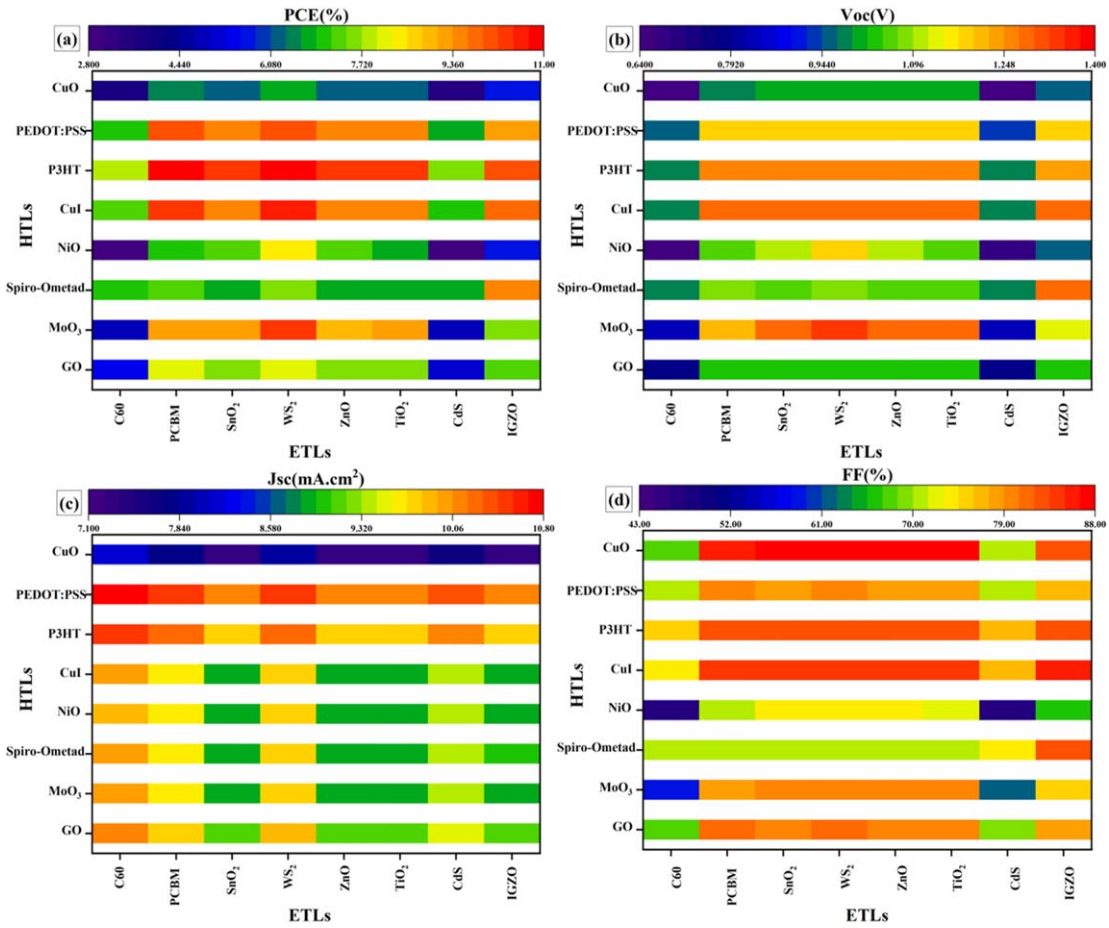

Figure 5. Impact of various ETLs and HTLs in T_{CELL} on (a) PCE (b) V_{OC} (c) J_{SC} (d) FF.

compatibility and high charge recombination [45]. The results suggest that for optimal performance, CuI/PCBM and CuI/SnO_2 should be favored, as they provide the highest efficiencies (~24%–25% in B_{CELL}, ~11% in T_{CELL}). Conversely, CuO-based devices consistently exhibit the worst performance, with lower V_{OC}, J_{SC}, FF, and ultimately, reduced PCE. These findings emphasize the importance of selecting ETL/HTL pairs with optimal energy level alignment, high charge mobility, and minimal recombination losses.

3.5. Effect of the temperature on the upper and lower sub-cells

The semiconducting materials have always been found to be dependent on the temperature [48] ,which influences key photovoltaic parameters such as PCE, FF, V_{OC} and J_{SC} by affecting the mechanism of carrier generation, recombination and transport in the solar cell [49]. The relationship between V_{OC} and J_{SC} and the temperature is given by equation (8) [45]. In this section investigates the effect of the operating temperature on the upper and lower sub-cells within the temperature range of 300 K to 400 K. This analysis aims to provide valuable insight into the behavior of the cell under different thermal conditions [50].

$$V_{oc} = nV_T \ln\left(\frac{I_{\{P\}} + \quad I_{\{0\}}}{I_{\{0\}}}\right); J_{\{SC\}} \approx I_{\{P\}} \tag{8}$$

The variation in performance of the two sub-cells as a function of temperature is illustrated in figure 7. For the lower sub-cell, the results show that V_{OC} and PCE increase significantly from 0.9257 V to 1.02784 V and from 21.72% to 23.57% respectively, while FF decreases slightly from 77.02% to 75.73% and J_{SC} decreases slightly from 30.46 mA.cm^{-2} to 30.28 mA.cm^{-2} with increasing temperature. At higher temperatures, there is sufficient thermal energy is provided to generate more charge carriers and excitons. However, as excitons are neutral in nature, their higher concentration gradient leads to an increase in the series resistance of the device. As a consequence, V_{OC} increases, whereas the FF decreases due to increased recombination and resistance losses [51]. For the T_{CELL} (figure 7(a)), the FF increases steadily with temperature, which can be attributed to enhanced charge transport and reduced recombination at higher thermal energy levels. In addition, the PCE of the upper

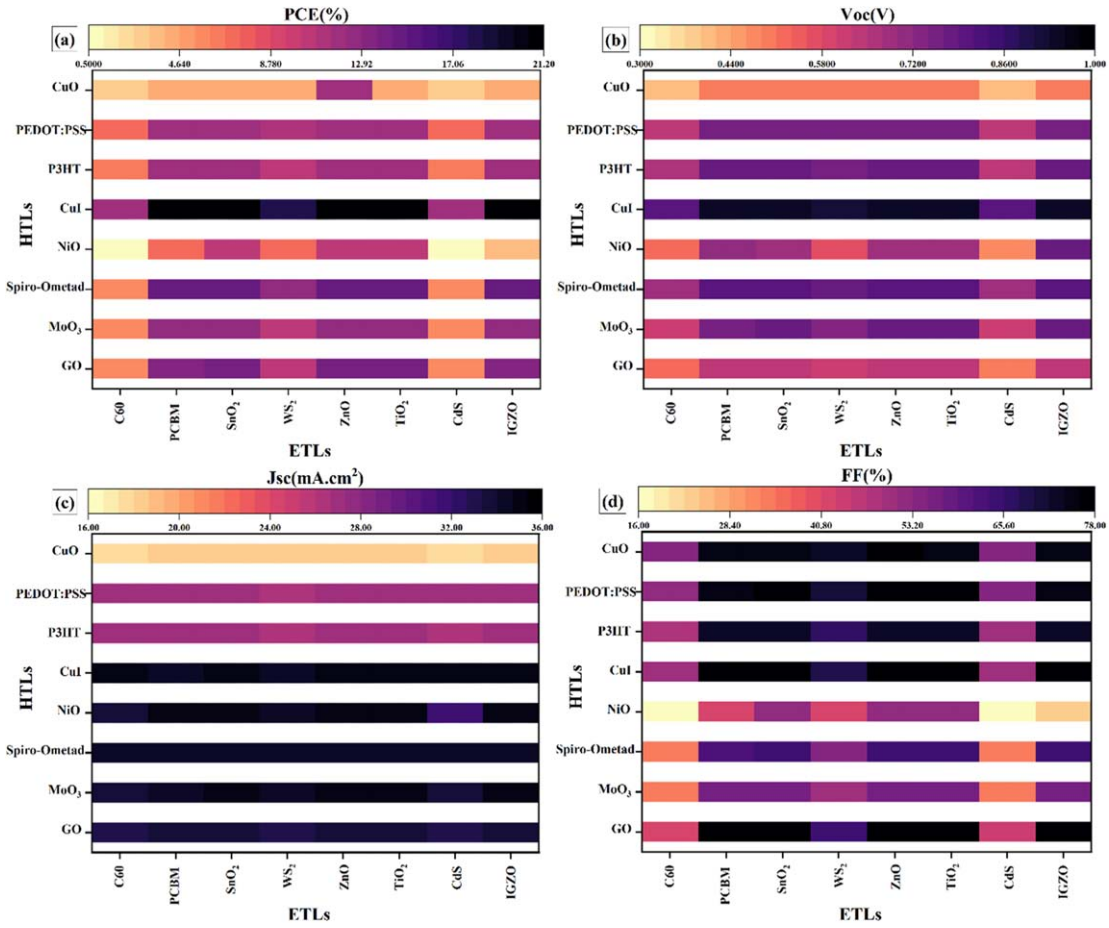

Figure 6. Impact of various ETLs and HTLs in B_{CELL} on (a) PCE (b) V_{OC} (c) J_{SC} (d) FF.

device showed a consistent increase of 0.016% over the entire temperature range, demonstrating its high stability even at elevated temperatures. Notably, the PCE of the device showed a slight increase of 0.01% at a temperature as high as 400 K, as shown in the results. On the other hand, V_{OC} showed only minor variations, with an initial increase from 1.14555 V to 1.15425 V between 300 K and 360 K, followed by a slight decrease to 1.14364 V at 400 K. The reduction in the open circuit voltage at higher temperatures can be attributed to an increase in the reverse saturation current density (J_o). This increase is mainly due to two factors: a decrease in the semiconductor bandgap and an increase in the intrinsic carrier concentration. These combined effects lead to the slight decrease in V_{OC} observed at elevated temperatures [52, 53].

The contrasting behavior of FF in the two sub-cells suggests that the top cell benefits from improved charge extraction and reduced recombination with increasing temperature, while the bottom cell suffers from higher resistive losses and interfacial degradation. This highlights the importance of optimizing the material interfaces and transport layers in the bottom cell to mitigate the impact of thermal effects on device performance.

3.6. Effect of shunt and series resistance on sub cells

The design of high-performance solar cells requires minimizing the series resistance (R_S) and maximizing the shunt resistance (R_{SH}). The series resistance (Rs) represents the internal resistance to current flow in the solar cell and has a direct effect on the fill factor (FF) and short-circuit current (J_{SC}), The Shockley equations (10) and (11), formulated by William Shockley, describe the current–voltage (J-V) behavior of an ideal solar cell taking into account the effects of R_S and R_{SH} [10].

$$Voc = \left(\frac{\mathrm{nKT}}{\mathrm{q}}\right)\ln\left[\frac{J_{ph}}{J_0}\left(1 - \frac{Voc}{J_{ph}R_{sh}}\right)\right] \tag{9}$$

$$Jsc = J_0 - J_{ph}\left[e^{\frac{q(V-JR_s)}{nKT}} - 1\right] - \frac{V - JR_s}{R_{sh}} \tag{10}$$

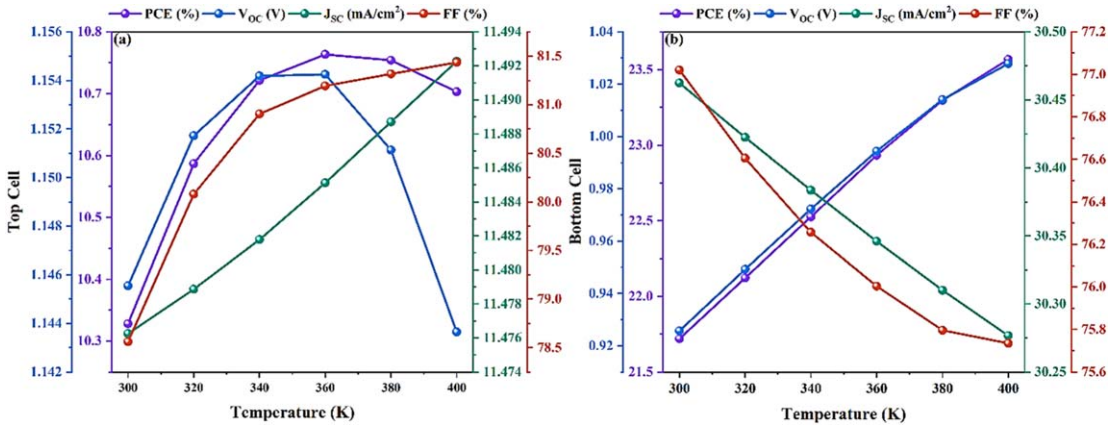

Figure 7. Temperature effect on output parameters PCE, V_{OC}, J_{SC} and FF, (a) upper cell, (b) lower cell.

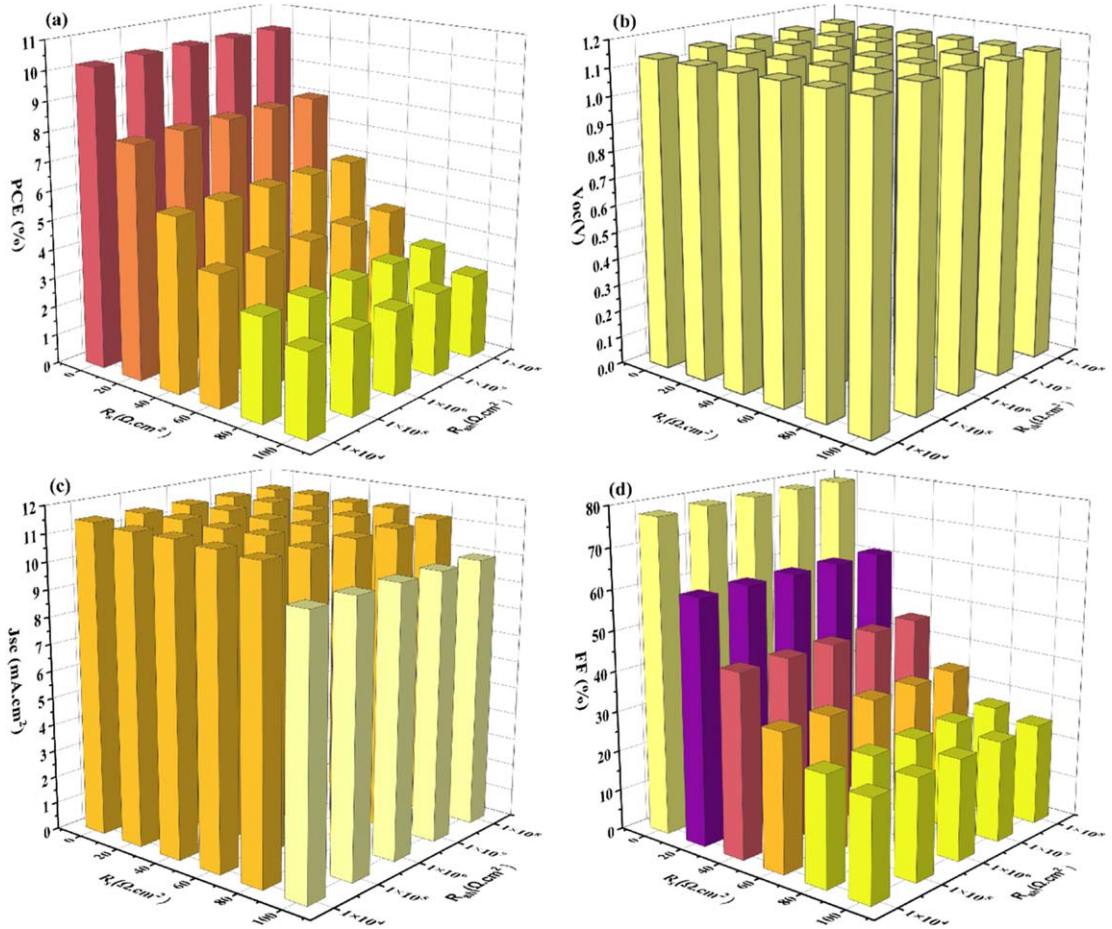

Figure 8. Impact of Series and Shunt Resistances on Top sub-cell Performance metrics.

$$FF = \frac{P_{\max}}{V_{oc} J_{sc}} \tag{11}$$

$$PCE = \frac{V_{oc} \times J_{sc} \times FF}{P_{in}} \tag{12}$$

Figures 8 and 9 shows the variation in performance of the two sub-cells as a function of series and shunt resistance. The open-circuit voltages of the two sub-cells are not affected by variations in R_{SH} and R_S. The short-circuit current (J_{SC}) of the two sub-cells remains relatively stable at high values of R_{SH}, but decreases with

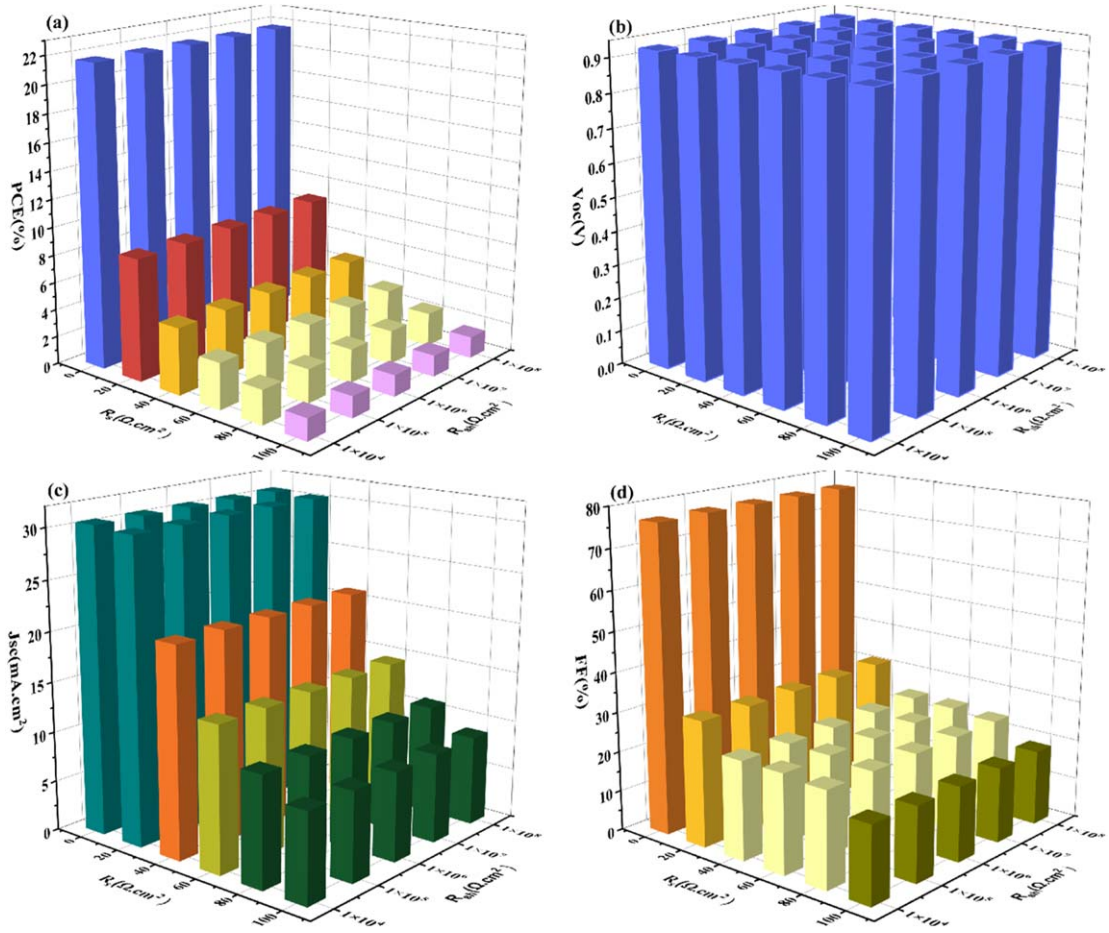

Figure 9. Impact of Series and Shunt Resistances on Bottom sub-cell Performance metrics.

increasing R_s, from 30.5 mA cm^{-2} to 8.92 mA cm^{-2} for the lower cell. This observation is consistent with Shockley's equations (9), (10).

The fill factor (FF) increases slightly with R_{SH}, rising from 76.8% to 77% for the lower cell and reaching 78.6% for the upper cell. On the other hand, it falls significantly with increasing R_S, from 76.8% to 19.3% for the lower cell, and drops to 25.1% when R_S reaches 100 Ω.cm^2 as confirmed by equation (11). The combination of the decrease in J_{SC} and FF leads to a reduction in the overall PCE, as shown by equation (12). For the upper cell, the efficiency remains stable at around 21.7% at high values of R_{SH}, but drops to 1.59% with increasing Rs for the lower cell. Efficiency reaches a relatively high level of 10.2% at high values of R_{SH}, but drops to 2.85% as R_S increases for the top cell. By minimizing R_S and increasing R_{SH}, it is possible to improve short-circuit current (J_{SC}), open-circuit voltage (V_{OC}), fill factor (FF) and power conversion efficiency (PCE), leading to more efficient and higher performing solar cells [35].

4. Tandem cell simulation

This section describes the proposed structure for the polymer tandem solar cell (TSC) shown in figure 1.

The proposed design integrates a wide bandgap top cell with a narrower bandgap bottom cell. Table 5 presents a detailed overview of the photovoltaic (PV) performance parameters. Figure 10 show the simulation results, including the J-V curves and EQE for the tandem solar cell (TSC) and the two sub-cells. The corresponding PV parameters are as follows (V_{OC}) of 2.0721 V, a short circuit current density (J_{SC}) of 11.685 mA cm^{-2}, a fill factor (FF) of 82.823% and a power conversion efficiency (PCE) of 20.054%. The results indicate that the lower current between the sub-cells regulates the tandem current, while the tandem V_{OC} is almost equal to the sum of the V_{OC} values of the individual cells.

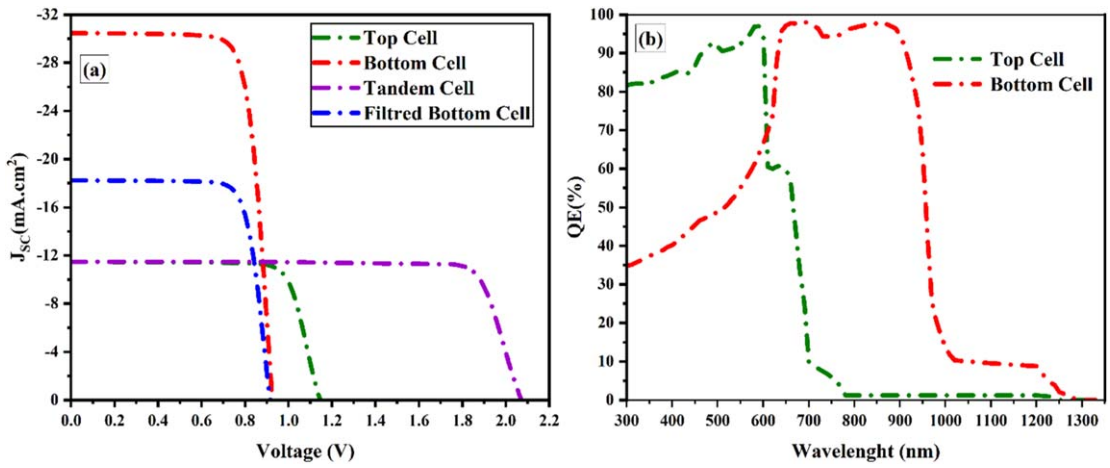

Figure 10. (a) JV curve and (b) EQE plot for top cell, bottom cell and tandem cell.

Table 5. Display of the PV metrics of various cells.

PV parameters	J_{SC} (mA.cm^2)	V_{OC} (v)	FF (%)	PCE (%)
Bottom Cell	30.462	0.9257	77.02	21.72
Filtred Bottom Cell	18.24	0.915	78.02	20.09
Top Cell	11.47	1.1455	78.56	10.33
Tandem	11.685	2.0721	82.823	20.054

Table 6. A state-of-the-art comparison between OSC/OSC TSC PV metrics and some TSCs.

PCE [%]	V_{OC} [V]	J_{SC} [mA cm^{-2}]	FF [%]	Bottom absorber layer	Top absorber layer	References
19	1.69	15	74.8	PTB7-Th:BTPSeV-4F (1.21 eV)	PM6 :O1-Br (1.58 eV)	[54]
17.3	1.64	14.4	73.3	PTB7-Th:O6T-4F (1.24 eV)	PBDB-T :F-M (1.72 eV)	[55]
15.9	1.66	14.1	68	PM6: SFT8-4F (1.31)	PCE-10:BT-CIC:BEIT-4F (1.64 eV)	[55]
15	1.6	13.6	69	PTB7-Th:PCDTBT:IEICO-4F (1.32 eV)	PBDB-T-2F:TfIF-4FIC (1.65 eV)	[55]
19.5	1.912	14.2	72	PBDB-TF: ITCC (1.32 eV)	PBDB-TF:BTP-eC11 (1.74 eV)	[55]
18.7	1.883	14	70.9	PM6: CH1007: PC71BM (1.36 eV)	D18: F-ThBr (1.73 eV)	[56]
15.2	1.61	12.9	73	PM6: Y6 (1.37 eV)	PV2000: PCBM (1.73 eV)	[55]
19.6	2.03	13	74.2	PBDB-TF:HDO-4Cl:BTP-eC9 (1.39 eV)	PB2:GS-ISO (1.78 eV)	[57]
17.9	2	11.7	76.3	PM6:PY-IT (1.45 eV)	PM7:PIDT (1.76 eV)	[12]
20.054	2.0721	11.685	82.823	PM6:Y6 (1.4 eV)	PM7:PIDT (1.76 eV)	This work

The quantum efficiency for the top cell starts at around 40% at 300 nm and increases with increasing wavelength, peaking at around 70% at around 600 nm. It then drops sharply after 700 nm, indicating that the top cell is optimized to absorb light mainly in the lower part of the visible spectrum (300–700 nm).

The bottom cell shows high quantum efficiency over a wider range of wavelengths, particularly from around 600 nm to 1000 nm, with QE approaching 100%. This suggests that the bottom cell is designed to absorb light in the higher part of the visible spectrum and into the near infrared (700–1000 nm). Its efficiency drops sharply after 1000 nm. The top cell absorbs primarily shorter wavelengths, while the bottom cell absorbs longer wavelengths, maximizing energy capture over a broader spectrum, demonstrating the complementary absorption profiles of the tandem cells.

5. Comparison with experimental previous studies

We present a comparative study between our proposed tandem cell configuration and other contenders among thin-film tandem solar cells, highlighting the state-of-the-art in various materials and cell architectures. Table 6 displays the performance metrics of tandem solar cells, with power conversion efficiencies (PCE) ranging from

15% to 19.6%. The highest performances are generally associated with cells featuring higher bandgaps for the top layer (E_g, T_{CELL}) and an optimal balance among other parameters. Cells with bottom layer bandgaps (E_g, B_{CELL}) ranging from 1.21 eV to 1.45 eV, and top layer bandgaps (E_g, T_{CELL}) from 1.58 eV to 1.80 eV, indicate that optimal performance is often achieved with well-matched bandgaps, which enhance light absorption and charge transfer efficiency. Cells exhibiting high open-circuit voltages (V_{OC}) of 2.02 V and 2.01 V respectively, along with a superior fill factor (FF), demonstrate excellent band alignment and improved charge extraction efficiency. Our proposed configuration stands out with exceptional performance, achieving the highest PCE, V_{OC}, and FF, while maintaining a competitive short-circuit current density (J_{SC}). These results underscore the remarkable efficiency and potential of our design relative to the other listed tandem solar cells.

6. Conclusion

In this work, a 2 T monolithic polymer/polymer tandem solar cell (TSC) model was proposed, with individual sub-cells calibrated based on experimental investigations. The calibration resulted in power conversion efficiencies (PCE) of 10.33% for the front cell and 21.72% for the back cell. We conducted an in-depth study of various factors affecting TSC performance, including the band alignment between the top and bottom cells, and the thickness and defect density of the organic active layers. In addition, the effect of electron transport layers (ETLs) and hole transport layers (HTLs) on the performance of both the top cell (T_{CELL}) and the bottom cell (B_{CELL}) was analyzed.

Further investigations examined the effects of temperature, shunt resistance and series resistance on the two sub-cells. The resulting model gave a short circuit current density (J_{SC}) of 11.685 mA cm^{-2}, an open circuit voltage (V_{OC}) of 2.0721 V, a fill factor of 82.823% and a PCE of 20.054%. These results indicate that our proposed design has the potential to advance flexible, environmentally friendly and highly efficient tandem solar cells.

However, this work is limited by the assumptions made in the SCAPS-1D simulation, including the uniformity of material properties and the idealized nature of the interfaces. Additionally, the absence of experimental validation for the complete tandem structure represents a challenge for real-world implementation, as practical considerations such as fabrication complexities, long-term stability, and scalability were not fully addressed. Future research should focus on experimentally validating the proposed model and exploring advanced materials and fabrication techniques to overcome these limitations.

Acknowledgments

The authors wish to thank the Directorate General of Scientific Research and Technological Development (DGRSDT, MESRS, Algeria) for their financial support. We thank Professor Burgelman from Ghent University for providing the SCAPS-1D software for the simulation work.

Data availability statement

All data that support the findings of this study are included within the article (and any supplementary files).

Funding

This research did not receive any specific grant from funding agencies in the public, commercial, or not-for-profit sectors.

Declaration of competing interest

The authors declare that no funds, grants, or other support were received during the preparation of this manuscript.

Ethical approval

All the authors declare that the manuscript does not have studies on human subjects, human data or tissue, or animals.

ORCID iDs

Samia Moulebhar https://orcid.org/0009-0008-2574-749X
Chahrazed Bendenia https://orcid.org/0000-0001-6994-3902
Souhila Bendenia https://orcid.org/0000-0003-4788-7238
Hanaa Merad-Dib https://orcid.org/0000-0002-9711-9272
Sid Ahmed Khantar https://orcid.org/0009-0004-8010-9619
Sarra Merabet https://orcid.org/0009-0002-8246-4070

References

[1] Okil M, Salem M S, Abdolkader T M and Shaker A 2022 From crystalline to low-cost silicon-based solar cells: a review *Silicon* **14** 1895–911
[2] Alanazi T I and El Sabbagh M 2023 Proposal and design of flexible All-Polymer/CIGS tandem solar cell *Polymers* **15** 1823
[3] Department of Physics, FECS, Ziane Achour University, 17000 Djelfa, Algeria, Hafaifa L, Maache M, Department of Physics, FECS, Ziane Achour University, 17000 Djelfa, Algeria, Bouabdelli M W and et Laboratory for analysis and Control of Energy Systems and Electrical Networks, Faculty of Technology, Amar Telidji University, BP 37G, 03000 Laghouat, Algeria 2024 Improving the performance of CZTS/CZTSSe tandem thin film solar cell *J. Nano- Electron. Phys.* **16** 02018-1-02018-6
[4] Dong S, Jia T, Zhang K, Jing J and Huang F 2020 Single-component non-halogen solvent-processed high-performance organic solar cell module with efficiency over 14% *Joule* **4** 2004–16
[5] Sun R *et al* 2019 A multi-objective optimization-based layer-by-layer blade-coating approach for organic solar cells: rational control of vertical stratification for high performance *Energy Environ. Sci.* **12** 3118–32
[6] Søndergaard R, Hösel M, Angmo D, Larsen-Olsen T T and Krebs F C 2012 Roll-to-roll fabrication of polymer solar cells *Mater. Today* **15** 36–49
[7] Yuan J *et al* 2019 Single-junction organic solar cell with over 15% efficiency using fused-ring acceptor with electron-deficient core *Joule* **3** 1140–51
[8] Yasodharan R, Senthilkumar AP, Mohankumar P, Ajayan J and Sivabalakrishnan R 2020 Investigation and influence of layer composition of tandem perovskite solar cells for applications in future renewable and sustainable energy *Optik* **212** 164723
[9] Sun R *et al* 2020 A layer-by-layer architecture for printable organic solar cells overcoming the scaling lag of module efficiency *Joule* **4** 407–19
[10] Cui Y *et al* 2021 Single-junction organic photovoltaic cell with 19% efficiency *Adv. Mater.* **33** 2102420
[11] Moulebhar S, Bendenia C, Merad-Dib H, Bendenia S, Merabet S and Khantar S A 2024 Hybrid optimization approach using multiobjective genetic algorithm NSGA-II, SCAPS-1D simulation, and response surface methodology for organic solar cell analysis *Physica Status Solidi (a)* 2400654
[12] Ma Q, Jia Z, Meng L, Yang H, Zhang J, Lai W, Guo J, Jiang X, Cui C and Li Y 2023 17.87% efficiency all-polymer tandem solar cell enabled by complementary absorbing polymer acceptors *Adv. Funct. Materials* **33** 2210733
[13] Wang J, Zheng Z, Zu Y, Wang Y, Liu X, Zhang S, Zhang M and Hou J 2021 A tandem organic photovoltaic cell with 19.6% efficiency enabled by light distribution control *Adv. Mater.* **33** 2102787
[14] Li C *et al* 2021 Non-fullerene acceptors with branched side chains and improved molecular packing to exceed 18% efficiency in organic solar cells *Nat. Energy* **6** 605–13
[15] Jia Z *et al* 2021 High performance tandem organic solar cells via a strongly infrared-absorbing narrow bandgap acceptor *Nat. Commun.* **12** 178
[16] Alanazi T I, Alanazi A, Touti E, Agwa A M, Kraiem H, Alanazi M, Alanazi A M and El Sabbagh M 2023 Proposal and numerical analysis of organic/Sb2Se3 all-thin-film tandem solar cell *Polymers* **15** 2578
[17] Chen X *et al* 2020 Efficient and reproducible monolithic perovskite/organic tandem solar cells with low-loss interconnecting layers *Joule* **4** 1594–606
[18] Todorov T, Gunawan O and Guha S 2016 A road towards 25% efficiency and beyond: perovskite tandem solar cells *Mol. Syst. Des. Eng.* **1** 370–6
[19] Ameri T, Li N and Brabec C J 2013 Highly efficient organic tandem solar cells: a follow up review *Energy Environ. Sci.* **6** 2390
[20] Zhang G *et al* 2022 Efficient all-polymer solar cells enabled by interface engineering *Polymers* **14** 3835
[21] Zhang Z, Yang Y, Yao J, Xue L, Chen S, Li X, Morrison W, Yang C and Li Y 2017 Constructing a strongly absorbing low-bandgap polymer acceptor for high-performance all-polymer solar cells *Angew. Chem.* **129** 13688–92
[22] Alanazi T I, Shaker A, Gad M and Okil M 2024 Optimization of all-polymer/Sb_2Se_3 tandem solar cells for enhanced efficiency: a comprehensive TCAD modeling approach *Phys. Scr.* **99** 065516
[23] Prajapati U K, Soni E, Solanki M and Rani J 2023 Enhancing the efficiency of PM6:Y6 bulk-heterojunction organic solar cells through SCAPS simulation optimization *Chin. J. Phys.* S0577907323002939
[24] Hossain M K *et al* 2023 Design insights into La_2NiMnO_6-based perovskite solar cells employing different charge transport layers: DFT and SCAPS-1D frameworks *Energy Fuels* **37** 13377–96
[25] Srivastava P, Sadanand, Rai S, Lohia P, Dwivedi D K, Qasem H, Umar A, Akbar S, Algadi H and Baskoutas S 2022 Theoretical study of perovskite solar cell for enhancement of device performance using SCAPS-1D *Phys. Scr.* **97** 125004
[26] Zein W, Alanazi T I, Saeed A, Salah M M and Mousa M 2024 Proposal and design of organic/CIGS tandem solar cell: Unveiling optoelectronic approaches for enhanced photovoltaic performance *Optik* **302** 171719
[27] Tokmoldin N, Hosseini S M, Raoufi M, Phuong L Q, Sandberg O J, Guan H, Zou Y, Neher D and Shoaee S 2020 Extraordinarily long diffusion length in PM6:Y6 organic solar cells *J. Mater. Chem.* A **8** 7854–60
[28] Yang J, Chen W, Yu B, Wang H and Yan D 2012 Organic tandem solar cell using active inter-connecting layer *Org. Electron.* **13** 1018–22
[29] Hafaifa L, Maache M, Allam Z and Zebeir A 2024 Simulation and performance analysis of CdTe thin film solar cell using different Cd-free zinc chalcogenide-based buffer layers *Results in Optics* **14** 100596
[30] Kim K, Gwak J, Ahn S K, Eo Y-J, Park J H, Cho J-S, Kang M G, Song H-E and Yun J H 2017 Simulations of chalcopyrite/c-Si tandem cells using SCAPS-1D *Sol. Energy* **145** 52–8

[31] Selmane N, Cheknane A and Hilal H S 2024 A new CsPbI2Br/CuZnSnSSe/Si tandem solar cell with higher than 32% efficiency *Micro and Nanostructures* **194** 207940
[32] Chen S, Feng L, Jia T, Jing J, Hu Z, Zhang K and Huang F 2021 High-performance polymer solar cells with efficiency over 18% enabled by asymmetric side chain engineering of non-fullerene acceptors *Sci. China Chem.* **64** 1192–9
[33] Khan M R and Jarząbek B 2023 Optimization and efficiency enhancement of modified polymer solar cells *Polymers* **15** 3674
[34] El-Demsisy H A, Shaker A, Asham M D, Ahmed I S and Abdolkader T M 2024 Efficiency boosting of 4-T bifacial dual-textured perovskite/perl silicon tandem solar cells: process and device TCAD simulation study *Silicon* **16** 5337–53
[35] Ravidas B K, Das A, Agnihotri S K, Pandey R, Madan J, Hossain M K, Roy M K and Samajdar D P 2024 Design principles of crystalline silicon/CsGeI3 perovskite tandem solar cells using a combination of density functional theory and SCAPS-1D frameworks *Sol. Energy Mater. Sol. Cells* **267** 112688
[36] Salem M S, Okil M, Shaker A, Abouelatta M, Salah M M, Al-Dhlan K A and Gad M 2024 TCAD-Based design and optimization of flexible Organic/Si tandem solar cells *Crystals* **14** 584
[37] Shrivastav N, Kashyap S, Madan J, Mohammed M K A, Hossain M K and Pandey R 2023 An efficient all-perovskite two terminal monolithic tandem solar cell with improved photovoltaic parameters: a theoretical prospect *Optik* **281** 170821
[38] Shrivastav N, Madan J, Pandey R and Shalan A E 2021 Investigations aimed at producing 33% efficient perovskite–silicon tandem solar cells through device simulations *RSC Adv.* **11** 37366–74
[39] Hossain M K, Toki G F I, Kuddus A, Rubel M H K, Hossain M M, Bencherif H, Rahman M F, Islam M R and Mushtaq M 2023 An extensive study on multiple ETL and HTL layers to design and simulation of high-performance lead-free CsSnCl3-based perovskite solar cells *Sci. Rep.* **13** 2521
[40] Rai S, Pandey B K and Dwivedi D K 2020 Modeling of highly efficient and low cost CH3NH3Pb(I1-xClx)3 based perovskite solar cell by numerical simulation *Opt. Mater.* **100** 109631
[41] Rai S, Pandey B K and Dwivedi D K 2021 Designing hole conductor free tin–lead halide based all-perovskite heterojunction solar cell by numerical simulation *J. Phys. Chem. Solids* **156** 110168
[42] Abena A M N, Ngoupo A T, Abega F X A and Ndjaka J M B 2022 Numerical investigation of solar cells based on hybrid organic cation perovskite with inorganic HTL via SCAPS-1D *Chin. J. Phys.* **76** 94–109
[43] Puente-López E and Pal M 2023 Numerical simulation and optimization of physical properties for high efficiency CuSbS2 thin film solar cells *Optik* **272** 170233
[44] Hafaifa L, Maache M and Bouabdelli M W 2024 Improved performance of CdTe thin-film solar cell through key parameters *J Theor Appl Phys.* **18**
[45] AlZoubi T, Mourched B, Al Gharram M, Makhadmeh G and Abu Noqta O 2023 Improving photovoltaic performance of hybrid organic-inorganic MAGeI3 perovskite solar cells via numerical optimization of carrier transport materials (HTLs/ETLs) *Nanomaterials* **13** 2221
[46] Ghosh R, Singh A and Agarwal P 2023 Study on effect of different HTL and ETL materials on the perovskite solar cell performance with TCAD simulator *Mater. Today Proc.* S221478532303554X
[47] El Arfaoui Y, Khenfouch M and Habiballah N 2024 Optimization of all Pb-free perovskite CsGeI3/FASnI3 tandem solar device with 30.42% efficiency: numerical simulation using SCAPS *Optik* **300** 171638
[48] Pathania A, Madan J, Pandey R and Sharma R 2020 Effect of structural and temperature variations on perovskite/Mg2Si based monolithic tandem solar cell structure *Appl. Phys.* A **126** 580
[49] Uddin M S, Al Mashud M A, Toki G F I, Pandey R, Zulfiqar M, Saidani O, Chandran K, Ouladsmane M and Hossain M K 2023 Lead-free Ge-based perovskite solar cell incorporating TiO2 and Cu2O charge transport layers harnessing over 25% efficiency *J. Opt.* **53** 3726–42
[50] Hafaifa L, Maache M, Rabhi S, Allam Z, Gouchida Z I, Benbouzid Y, Zebeir A and Adjouz R 2024 Enhanced CZTSSe thin-film solar cell efficiency: key parameter analysis *Physica Status Solidi (a)* **222** 2400332
[51] Subudhi P and Punetha D 2023 Pivotal avenue for hybrid electron transport layer-based perovskite solar cells with improved efficiency *Sci. Rep.* **13** 19485
[52] Ahmad I, Hayat K, Ashraf M, Imran M and Shah S K 2023 SCAPS-based simulation analysis of device parameters of ZnO-inverted polymer solar cells *Opt. Quant. Electron.* **55** 345
[53] Sharma A K, Chourasia N K, Jha P K, Kumar R, Kumar M and Chourasia R K 2023 Characteristic features and performance investigations of a PTB7:PC71BM/PFN:Br pure organic solar cell using SCAPS-1D *J. Electron. Mater.* **52** 4302–11
[54] Jia Z *et al* 2023 Near-infrared absorbing acceptor with suppressed triplet exciton generation enabling high performance tandem organic solar cells *Nat. Commun.* **14** 1236
[55] Almora O *et al* 2021 Device performance of emerging photovoltaic materials (version 1) *Adv. Energy Mater.* **11** 2002774
[56] Almora O *et al* 2021 Device performance of emerging photovoltaic materials (version 2) *Adv. Energy Mater.* **11** 2102526
[57] Wang J *et al* 2023 Binary organic solar cells with 19.2% efficiency enabled by solid additive *Adv. Mater.* **35** 2301583